

# Crystalline grain engineered CsPbIBr<sub>2</sub> films for indoor photovoltaics

Paheli Ghosh<sup>a</sup>, Jochen Bruckbauer<sup>b</sup>, Carol Trager-Cowan<sup>b</sup> and Lethy Krishnan Jagadamma<sup>a\*</sup>

<sup>a</sup>Energy Harvesting Research Group, School of Physics & Astronomy, SUPA, University of St Andrews, St Andrews, KY16 9SS, United Kingdom

<sup>b</sup>Department of Physics, SUPA, University of Strathclyde, Glasgow, G4 0NG, United Kingdom

Email: [lkj2@st-andrews.ac.uk](mailto:lkj2@st-andrews.ac.uk)

## Abstract

Indoor photovoltaic devices have garnered profound research attention in recent years due to their prospects of powering ‘smart’ electronics for the Internet of Things (IoT). Here it is shown that all-inorganic Cs-based halide perovskites are promising for indoor light harvesting due to their wide bandgap matched to the indoor light spectra. Highly crystalline and compact CsPbIBr<sub>2</sub> perovskite based photovoltaic devices have demonstrated a power conversion efficiency (PCE) of 14.1% under indoor illumination of 1000 lux and 5.9% under 1 Sun. This study revealed that a reduction in grain misorientation, as well as suppression of defects in the form of metallic Pb in the perovskite film are crucial for maximising the photovoltaic properties of CsPbIBr<sub>2</sub> based devices. It was demonstrated that a pinhole free CsPbIBr<sub>2</sub>/Spiro-OMeTAD interface preserves the perovskite  $\alpha$  phase and enhances the air stability of the CsPbIBr<sub>2</sub> devices. These devices, despite being unencapsulated, retained >55% of the maximum PCE even when stored under 30% relative humidity for a shelf-life duration of 40 days and is one of the best stability data reported so far for CsPbIBr<sub>2</sub> devices.

## Keywords

All-inorganic perovskite, EBSD, grain misorientation, Internet of Things, mixed halides, XPS

## 1. Introduction

The constant decrease in energy requirements for the Internet of Things (IoT) has resulted in immense research being focussed on self-powered wireless devices. The self-powering feature is expected to circumvent the issues with energy storage and hence, contribute towards the growth and sustainability of IoT technology. Many of these wireless devices are expected to be used indoors, with minimal power requirement in the range of micro to milliwatts and

hence, efficient, and reliable indoor photovoltaics (IPV) would serve as the suitable power source. IPVs suitable for powering the sensors should not only have high power conversion efficiency (PCE) but must also encompass attributes such as low cost, flexibility, robustness and be easily processable from earth-abundant materials. Though commercial crystalline silicon solar cells are suitable for harvesting solar radiation, the relatively narrow bandgap (1.1 eV), complex and energy-intensive fabrication requirements and high trap-assisted recombination under low-intensity illumination limit their application as indoor photovoltaics [1,2]. Hence the development of alternate absorber materials for IPVs is of paramount importance to sustainably support the rapidly growing IoT technology. These absorber materials should have wide bandgap (1.9 eV) and fewer defects since the indoor artificial light sources such as white light emitting diodes (LEDs) and fluorescent lamps (CFLs) primarily emit photons in the visible region (400 - 700 nm) and have lower intensity (0.1 - 1 mW cm<sup>-2</sup>) compared to the 1 Sun spectrum [3–5].

Hybrid halide perovskite semiconductors are promising for many optoelectronic applications owing to their favourable attributes of high charge carrier mobility, wide absorption spectrum, tunable bandgap, ease of device fabrication using solution-processed and vacuum deposition techniques and have demonstrated outstanding solar cell PCE of 25.5% under 1 Sun [6]. Among them, all inorganic halide perovskites such as CsPbX<sub>3</sub> (where X = Cl, Br or I) have a tunable bandgap ranging from 1.73 eV for CsPbI<sub>3</sub> to 2.3 eV for CsPbBr<sub>3</sub> and possess high thermal stability compared to their organic counterparts [7,8]. However, CsPbI<sub>3</sub> suffers from severe phase stability issues as the photo-active perovskite  $\alpha$ -phase is only stable at temperatures >330°C. The CsPbBr<sub>3</sub> shows appreciable stability but the large bandgap ( $E_g \sim 2.3$  eV) does not favour absorption in the visible region, thus, limiting their PV applications. The issues of pristine CsPbX<sub>3</sub> perovskites can be overcome by replacing some of the I<sup>-</sup> ions with Br<sup>-</sup> ions with amenability to tailoring of the bandgap.

CsPbIBr<sub>2</sub> with a bandgap of  $\sim 2.05$  eV [9] is suitable for indoor photovoltaics, integration in tandem devices and smart PV windows [10]. Previously, the application of CsPbIBr<sub>2</sub> has been explored in solar cells (with PCE ranging from 5-10%), photodetectors [11–14], and light emitting diodes [15]. Most of the reported studies on CsPbIBr<sub>2</sub> perovskite photovoltaics involved either high temperature annealing (ranging from 225°C - 360°C) of the active layer [9,16–24] or the charge transporting layers [9,16–18,21–24] or pre-heating the substrate (40 - 80 °C) [25]. This not only makes the fabrication process complex but also incompatible with flexible substrates and wearable technologies which are being widely explored in the IoT.

Moreover, these devices show appreciable hysteresis (ranging from 10 - 50%) and the air stability is often not explored. So far, the photovoltaic research on inorganic Cs-based perovskite solar cells has been primarily optimised for 1 Sun illumination with the application in indoor photovoltaics hardly investigated [26–29]. But the recent explosion in the IoT and indoor photovoltaics has necessitated the development of new semiconducting materials processable at temperatures low enough to be compatible with flexible substrates such as polyethylene terephthalate (PET) to maximise the chances of integration while implementing these devices as indoor light harvesters to power sensors in the IoT applications.

In this study, CsPbIBr<sub>2</sub> films with optimised surface features and crystalline properties were developed and the corresponding indoor photovoltaic devices demonstrated a champion PCE of 14% under white LED illumination and good air stability. These devices, without any encapsulation, retained more than 55% of the initial PCE even after 40 days of storage in 30% humidity. Detailed microstructural analysis using X-ray photoemission spectroscopy (XPS) and electron backscattered diffraction (EBSD) revealed that treatment of the perovskite layer using selected anti-solvents is not only effective in achieving the desired morphology but also in reducing the surface defects in the form of metallic Pb and the grain misorientation. The present study demonstrates the promising potential of all-inorganic Cs-based halide perovskites for indoor light harvesting.

## **2. Methods**

### **(a) Materials**

The chemicals used to prepare the CsPbIBr<sub>2</sub> perovskite solution [CsI and PbBr<sub>2</sub>, 99.999% purity] were used as received from Alfa Aesar. The SnO<sub>2</sub> solution (CAS 18282-10-5) for the electron transport layer (ETL) was bought from Alfa Aesar and diluted to the volume ratio 1:6.5 in deionized (DI) water prior to spin coating. The materials used for hole transport layer (HTL) solution preparation [2,2',7,7'-Tetrakis[N,N-di(4-methoxyphenyl)amino]-9,9'-spirobifluorene (Spiro-OMeTAD, >99% purity), 4-tert-butyl pyridine (tBP, 96% purity), lithium-bis(tri-fluoromethanesulfonyl)imide (Li-TFSI, 99.95% purity) and tris(2-(1H-pyrazol-1-yl)-4-tert-butylpyridine)cobalt(III) tri[bis(trifluoromethane)sulfonimide] (FK 209) were purchased from Ossila, Sigma Aldrich and Greatcellsolar Materials, respectively. Solvents such as dimethyl sulfoxide (DMSO, anhydrous, ≥99.9%), chlorobenzene (anhydrous, 99.8%), acetonitrile (anhydrous, 99.8%), and diethyl ether (anhydrous, ≥99.7%) were purchased from Sigma Aldrich.

## (b) Device fabrication

Patterned indium tin oxide (ITO)-coated glass substrates (glass/ITO with a sheet resistance of  $15 \Omega \square^{-1}$ ) were sequentially cleaned with sodium dodecyl sulphate (SDS), deionized water, acetone and isopropyl alcohol followed by plasma cleaning for 3 minutes with oxygen plasma in a Plasma Asher. A compact hole-blocking  $\text{SnO}_2$  ETL was spin-coated using 100  $\mu\text{L}$  of  $\text{SnO}_2$  solution [diluted to 1:6.5 volume ratio in DI water] at 3000 rpm for 30 seconds, followed by thermal annealing at  $150^\circ\text{C}$  for 30 minutes on a hot plate in ambient conditions inside a laminar flow fume hood. For the perovskite solution, CsI (1 M; 259.8 mg) and  $\text{PbBr}_2$  (1 M; 367.01 mg) as precursor materials were dissolved in anhydrous DMSO (1 mL) and stirred continuously for 2 hours at room temperature to achieve the desired  $\text{CsPbIBr}_2$  composition. The  $\text{CsPbIBr}_2$  perovskite solution was spin-coated on top of the  $\text{SnO}_2$  ETL using a two-step spin-coating procedure, the first step at 1000 rpm for 15 seconds followed by a second step at 4000 rpm for 45 seconds. 90  $\mu\text{L}$  of the mixed halide perovskite solution was used for spin coating, followed by treatment with 750  $\mu\text{L}$  of different anti-solvents (chlorobenzene and diethyl ether) during the last 15<sup>th</sup> second of the second spin coating step. These films were then annealed at  $150^\circ\text{C}$  on a hot plate for 15 minutes. The films turned brown immediately upon placing them on the hot plate. For the HTL, 65  $\mu\text{L}$  of a Spiro-OMeTAD solution [(72.3 mg of Spiro-OMeTAD, 28.8  $\mu\text{L}$  of tBP, 17.5  $\mu\text{L}$  of a Li-TFSI solution (520 mg Li-TFSI in 1 mL acetonitrile) and 29  $\mu\text{L}$  of a FK-209 solution (300 mg FK-209 in 1 mL acetonitrile)] in 1 mL chlorobenzene was spin coated at 4000 rpm for 30 seconds on the perovskite active layer. Before spin coating, the individual solutions for HTL were thoroughly mixed using the vortex mixer. The perovskite and HTL weighing, precursor solution preparation, stirring, perovskite active layer and HTL spin coating were undertaken in a nitrogen-filled glove box with relative humidity <15%. The glass/ITO/ $\text{SnO}_2$ /perovskite/Spiro-OMeTAD structures were wrapped in Aluminum foil and left overnight in a desiccator at room temperature for oxygen doping of Spiro-OMeTAD. Finally, a 60 nm thick Au electrode was thermally evaporated (chamber pressure  $3 \times 10^{-6}$  mbar) on top of the HTM to complete the perovskite solar cell device. An aperture mask was employed to determine the effective active area of the device as  $0.0646 \text{ cm}^2$ .

## (c) Films for characterization

The  $\text{CsPbIBr}_2$  films used for UV-Vis absorption spectroscopy, X-ray diffraction (XRD) and scanning electron microscopy (SEM) characterization were prepared on non-patterned ITO substrates (sheet resistance  $15 \Omega \square^{-1}$ ) using the same protocol for the active layer as mentioned

earlier. Prior to the perovskite spin coating, the substrates were thoroughly cleaned using the same cleaning procedure as followed during the device fabrication.

**(d) Characterization of CsPbIBr<sub>2</sub> perovskite films and devices**

The UV-Vis absorption spectra of CsPbIBr<sub>2</sub> perovskite thin films were recorded using a Cary 300 Bio Spectrometer over the wavelength range 300 – 800 nm.

The XRD patterns of the annealed perovskite films were collected using a Panalytical Empyrean X-ray diffractometer operating in Bragg-Brentano geometry with Cu K $\alpha_1$  radiation and an X'celerator RTMS detector. Data were acquired in the range 10° - 60° with a step size of 0.017° and a time per step of 147.955 seconds.

The surface morphology of the perovskite films was studied using a field-emission scanning electron microscope (Hitachi S4800 equipment). Electron backscattered diffraction (EBSD) measurements were performed in a variable pressure field emission gun scanning electron microscope (FEI Quanta 250) using a Nordlys EBSD detector from Oxford Instruments. The EBSD datasets from all samples were acquired at 20 kV and a sample tilt of 70° with respect to the normal of the incident electron beam. Data analysis was performed using the freely available Matlab-based toolbox MTEX [30].

The X-ray photoelectron spectra were acquired using a monochromated Al K $\alpha$  X-ray source (1486 eV, 10 mA emission at 150 W) for surface sensitive X-ray photoelectron spectroscopy (XPS) measurements. Charge neutralisation for insulating samples was achieved using a low energy electron flood source as required (FS40A, PreVac). Binding energy scale calibration was performed either using C-C in the C 1s photoelectron peak at 285 eV or using Au 4f<sub>7/2</sub> at 84 eV, else the Fermi level at 0 eV, of a clean gold reference sample. Analysis and curve fitting were performed using Shirley backgrounds with GL(50) Voigt-approximation peaks using CasaXPS [31].

Fourier transform infrared (FTIR) spectra were acquired using a Shimadzu IRAffinity 1S IR Spectrometer.

The photocurrent *versus* voltage (J-V) characteristics of the devices were evaluated under simulated AM 1.5G radiation (illumination intensity of 100 mW cm<sup>-2</sup>) by using a Sciencetech solar simulator (SS150-AAA) and a source meter (Keithley 2401). The solar cells were applied with a bias voltage sweep ranging from -0.20 V to 1.5 V, with a voltage step of 0.05 V and a delay time of 0.200 seconds. The light intensity was calibrated using a standard silicon solar

cell (ORIEL<sup>®</sup> PV Reference Cell System; Model number 91150V, certified by NREL) before undertaking J-V measurements.

The external quantum efficiency (EQE) of the PSCs were measured at zero bias by illuminating the devices with a monochromatic light source using a Xenon lamp in combination with a dual-grating monochromator from Bentham Instruments. The number of photons incident on the samples were calculated for each wavelength using a silicon photodiode calibrated by the National Physical Laboratory.

For the indoor measurements, four different light sources were used, namely, PRO-ELEC daylight white light-emitting diode (LED) (11 W, 6500K, intensity  $0.25 \text{ mW cm}^{-2}$ ), OSRAM cool white LED (8.5 W, 4000 K, intensity  $0.25 \text{ mW cm}^{-2}$ ), OSRAM warm white LED (806 lm Classic A 60, 8.5 W, 2700 K, intensity  $0.30 \text{ mW cm}^{-2}$ ), and a cool white compact fluorescent lamp (CFL) (23 W, 4000 K, intensity  $0.25 \text{ mW cm}^{-2}$ ). The luminous intensity was measured using a lux meter and all indoor lamps were set at 1000 lux illuminance.

### 3. Results and Discussion

#### (a) Photovoltaic properties

**Figure 1 (a)** shows the schematic of the n-i-p device architecture [Glass/ITO/SnO<sub>2</sub>/CsPbIBr<sub>2</sub>/Spiro-OMeTAD/Au] used in this study for the fabrication of the CsPbIBr<sub>2</sub> devices. Depending on their location inside buildings, various types of illumination are used indoors and hence, the photovoltaic properties of the optimised CsPbIBr<sub>2</sub> devices were characterised under different indoor lamps, namely, daylight white LED, warm white LED, cool white LED, and CFL. The emission spectra of the indoor illumination sources used in this study are shown in **Figure 1 (b)**. The maximum PCE demonstrated by the optimised devices were 9.4%, 8.7% and 6.3% under cool white LED, CFL and warm white LED, respectively. The photovoltaic parameters are summarised in Table S1 (Supplementary Information). The performance was found to be best in the case of daylight white LED due to the maximum spectral match between daylight white LED and the EQE spectra. The current density *versus* voltage (J-V) characteristics of the champion devices with the photovoltaic performance parameters measured under daylight white LED in forward and reverse scans are shown in **Figure 1 (c)**. These devices recorded champion photovoltaic parameters with a PCE of 14.1%, short circuit current ( $J_{SC}$ ), open circuit voltage ( $V_{OC}$ ) and fill factor (FF) as  $0.06 \text{ mA cm}^{-2}$ , 0.95 V and 61.6%, respectively, in reverse scan. The current density and PCE under a steady state voltage bias of 0.7 V are shown in **Figure 1 (d)**. A steady state PCE of 8.8% was

obtained under constant indoor light illumination of 1000 lux. **Figure 1 (e)** shows the corresponding J-V characteristics of the best device under 1 Sun condition. The PCE values were recorded as 5.3% and 5.9% in forward and reverse scans, respectively, with a very low hysteresis index of  $\sim 10\%$ . The corresponding photovoltaic parameters were recorded as  $8.51 \text{ mA cm}^{-2}$ ,  $1.01 \text{ V}$  and  $68.4\%$  for the  $J_{SC}$ ,  $V_{OC}$  and FF, respectively, in reverse scan. The stabilized current density and PCE were measured as  $\sim 4.3 \text{ mA cm}^{-2}$  and  $\sim 3.5\%$ , respectively, under  $0.8 \text{ V}$  bias under 1 Sun continuous illumination [**Figure 1 (f)**]. The longer stabilisation time for the  $J_{SC}$ /PCE under indoor light as compared to 1 Sun can be attributed to the higher hysteresis effect of these devices under low-intensity illumination as is evident from a comparison between Figure 1 (c) and Figure 1 (e). The higher J-V hysteresis effect in halide perovskite photodiodes under low-intensity illumination has been recently reported by Zhou *et al.* [32].

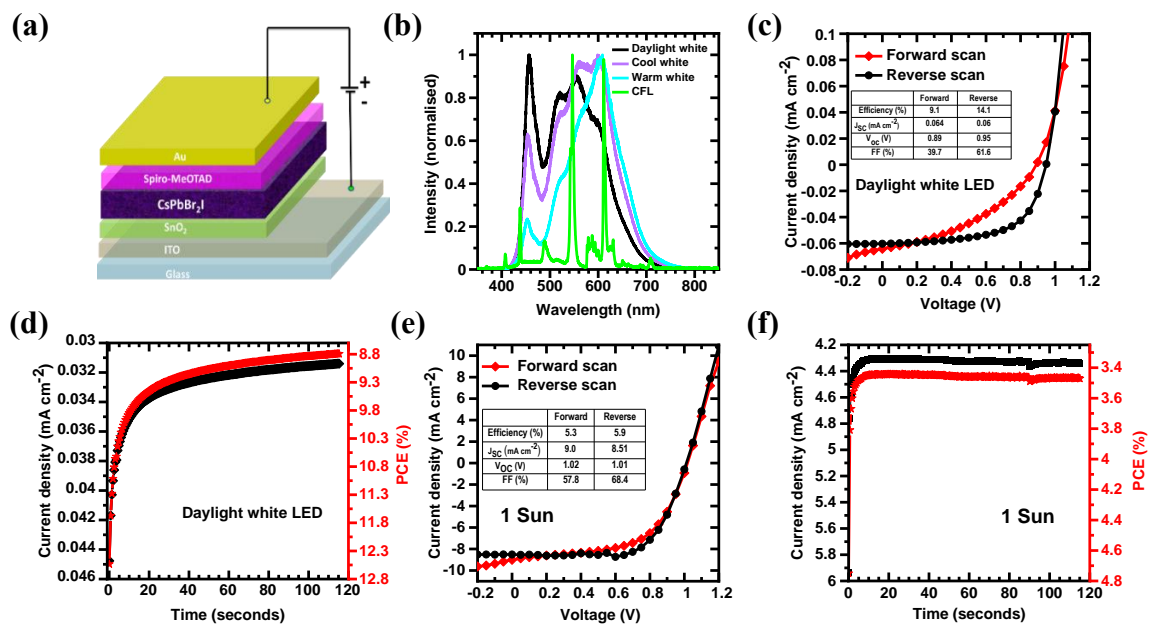


**Figure 1** (a) Device architecture of the n-i-p devices used in this study. (b) Spectra of the different indoor lamps used in this study. (c & e) Current density *versus* voltage curves for the best performing device in forward and reverse scans along with the photovoltaic parameters under (c) daylight white LED light and (e) 1 Sun illumination. (d & f) Steady state tracking of the current density and PCE under (d) daylight white LED (voltage bias  $\sim 0.7 \text{ V}$ ) and (f) 1 Sun condition (voltage bias  $\sim 0.8 \text{ V}$ ).

The performance reproducibility of the optimised CsPbIBr<sub>2</sub> devices under daylight white LED and 1 Sun is shown in **Figures 2 (a) and (b)**. Not only was the device performance reproducible but also the devices showed appreciable stability under ambient conditions as will be discussed in detail in the later sections. The external quantum efficiency (EQE) spectrum in **Figure 2 (c)** shows that the light harvesting ability of the CsPbIBr<sub>2</sub> photovoltaic devices approaches 60% in the bulk of the visible spectrum. The integrated J<sub>SC</sub> calculated from the EQE spectrum was 7.2 mA cm<sup>-2</sup> which is quite consistent with the J<sub>SC</sub> from the J-V measurements under 1 Sun. The CsPbIBr<sub>2</sub> films with these excellent photovoltaic properties were obtained after a series of optimisation steps as discussed in the next section.

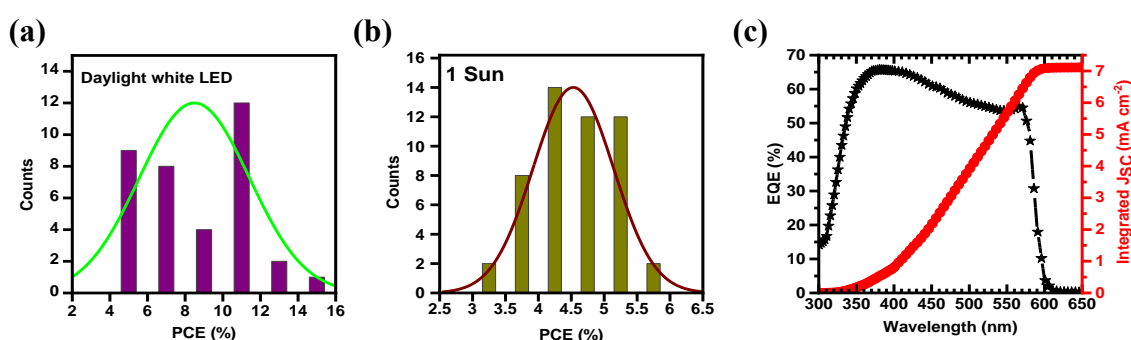


**Figure 2** (a & b) PCE distribution of 36 and 50 devices under daylight white LED (1000 lux) and 1 Sun illumination conditions, respectively. (c) External quantum efficiency spectrum with the integrated short circuit current for the CsPbIBr<sub>2</sub> perovskite devices.

### (b) Optimisation of CsPbIBr<sub>2</sub> films and photovoltaic devices

CsPbIBr<sub>2</sub> films were fabricated without and with anti-solvent treatment and systematically characterised using scanning electron microscopy (SEM), UV-Vis spectroscopy, X-ray diffraction (XRD), electron backscattered diffraction (EBSD) and X-ray photoelectron spectroscopy (XPS). The selected anti-solvents were diethyl ether and chlorobenzene. The UV-visible absorption spectra of freshly prepared CsPbIBr<sub>2</sub> perovskite films (thickness ~240 nm), irrespective of the anti-solvent treatment, show the same position of the absorption peak [**Figure 3 (a)**]. The absorption onset is observed at ~600 nm corresponding to a bandgap of ~2.09 eV and is in good agreement with previous reports [25,33–35] [Inset of Figure 3 (a) shows the Tauc plot]. The crystallinity of the pristine, chlorobenzene and diethyl ether treated CsPbIBr<sub>2</sub> perovskite films was investigated using XRD measurements. As can be seen from **Figure 3 (b)**, characteristic peaks at 15.24°, 21.52°, 30.42°, 34.14° and 37.37° corresponding to the (100), (110), (200), (210) and (211) planes of the cubic



$\alpha$ -phase CsPbIBr<sub>2</sub> perovskite structure are observed in all three cases [10,21,36]. The intensity of the (100) and (200) crystal planes is lowest in the case of chlorobenzene treated CsPbIBr<sub>2</sub> films, which suggests their inferior crystalline quality compared to the pristine and diethyl ether anti-solvent treated films. However, a closer look at the peaks shows the slight displacement of the (100) and (200) peak positions due to the usage of different anti-solvents [Figure S1]. Diethyl ether treatment has resulted in shifting the peak positions to lower angles, thus, suggesting an expansion of the crystal lattice. This implies the better incorporation of iodide ions into the CsPbIBr<sub>2</sub> crystal lattice.

The secondary electron (SE) images of the CsPbIBr<sub>2</sub> films obtained using scanning electron microscopy are shown in **Figure 3 (c)**. In the case of perovskite films fabricated without any anti-solvent treatment, discrete cube-like features are observed which appears to lack both continuity and surface coverage [**Figure 3 (c) (i)**]. The surface morphology becomes dense and compact and surface coverage improves upon anti-solvent treatment as can be seen from **Figures 3 (c) (ii) and (iii)**, though chlorobenzene treated CsPbIBr<sub>2</sub> films show the presence of randomly sized grain-like features ranging from 100 nm to 500 nm and the presence of pinholes [**Figure 3 (c) (ii)**]. A compact perovskite film with no pinholes and with grain-like domains ~500 nm in size is formed after diethyl ether treatment [**Figure 3 (c) (iii)**]. The term grain is used with caution here, as there is wide debate regarding grain and grain boundaries in the hybrid perovskites [37,38]. With these results from the optimisation of CsPbIBr<sub>2</sub> films, n-i-p photovoltaic devices were fabricated using chlorobenzene and diethyl ether as anti-solvents and characterised under both indoor artificial lights and outdoor 1 Sun spectra. Tables S2 and S3 summarize the corresponding photovoltaic performance parameters and the detailed description of the photovoltaic device optimization is given in the Supplementary Information.

Distribution of the photovoltaic parameters under 1 Sun for the devices fabricated without anti-solvent and with chlorobenzene and diethyl ether treatment are shown in **Figure 3 (d)**. Despite the incomplete surface coverage [Figure 3 (c) (i)], devices without anti-solvent treatment demonstrated a wide range of PCE values from ~2 - 5.9%. This suggests the presence of a thin layer of CsPbIBr<sub>2</sub> film on the surface which connects the discrete cube-like domains observed in the secondary electron images. Devices with diethyl ether treatment demonstrated higher PCE values with lower distribution range and best efficiency of 5.9%. Hence, the average hysteresis index was also lower in case of the diethyl ether treated devices (~17%) compared to those without any anti-solvent treatment (~21%). The V<sub>OC</sub> distribution was quite wide, ranging from ~0.75 V - 1.1 V in case of devices without anti-solvent, whereas majority

of the diethyl ether treated devices showed  $V_{OC}$  between 0.9 V and 1.1 V. The  $J_{SC}$  values were quite widespread, irrespective of sample preparation, however, the diethyl ether treated devices recorded higher  $J_{SC}$  on an average. The distribution of FF during forward scan was comparable in either case, ranging from ~40 - 58%, whereas the diethyl ether treated devices recorded considerably higher reverse scan FF (>60 - 80%) compared to devices without anti-solvent treatment (~55 - 70%). The comparatively better device performance with lesser variation in PCE values for devices fabricated with diethyl ether can be attributed to the improved perovskite crystallinity, grain size and surface coverage upon diethyl ether treatment [Figure 3 (c) (iii)]. This implies that diethyl ether anti-solvent treatment facilitates nucleation by rapidly reducing the precursors solubility which results in better crystallization and formation of large perovskite grains. Devices fabricated using chlorobenzene treatment recorded the lowest photovoltaic parameters due to the combination of inferior  $CsPbIBr_2$  crystal quality and the presence of pinholes [Figures 3 (b) and (c) (ii)]. **Figures 3 (e)** compares the J-V characteristics of the best performing  $CsPbIBr_2$  perovskite-based devices without anti-solvent, and with chlorobenzene and diethyl ether treatment under 1 Sun illumination. Devices without anti-solvent treatment showed a champion PCE of 5.9% in the reverse scan with  $J_{SC}$ ,  $V_{OC}$  and FF being  $7.9 \text{ mA cm}^{-2}$ , 1.14 V and 65.1%, respectively. The  $J_{SC}$  and FF improved with diethyl ether treatment, recording  $8.5 \text{ mA cm}^{-2}$  and 68.1%, respectively. The inferior performance of devices without anti-solvent treatment, coupled with their rapid degradation to the non-perovskite phase during 1 Sun measurement may be attributed to the formation of nucleation sites for phase segregation. Diffusion of  $Li^+$  ions from Spiro-OMeTAD upon air exposure or the interaction of mobile iodide species of the perovskite with Spiro-OMeTAD at the perovskite/hole-selective interface may facilitate growth of the non-perovskite phase due to the improper surface coverage which detrimentally affects the device stability [39–42].

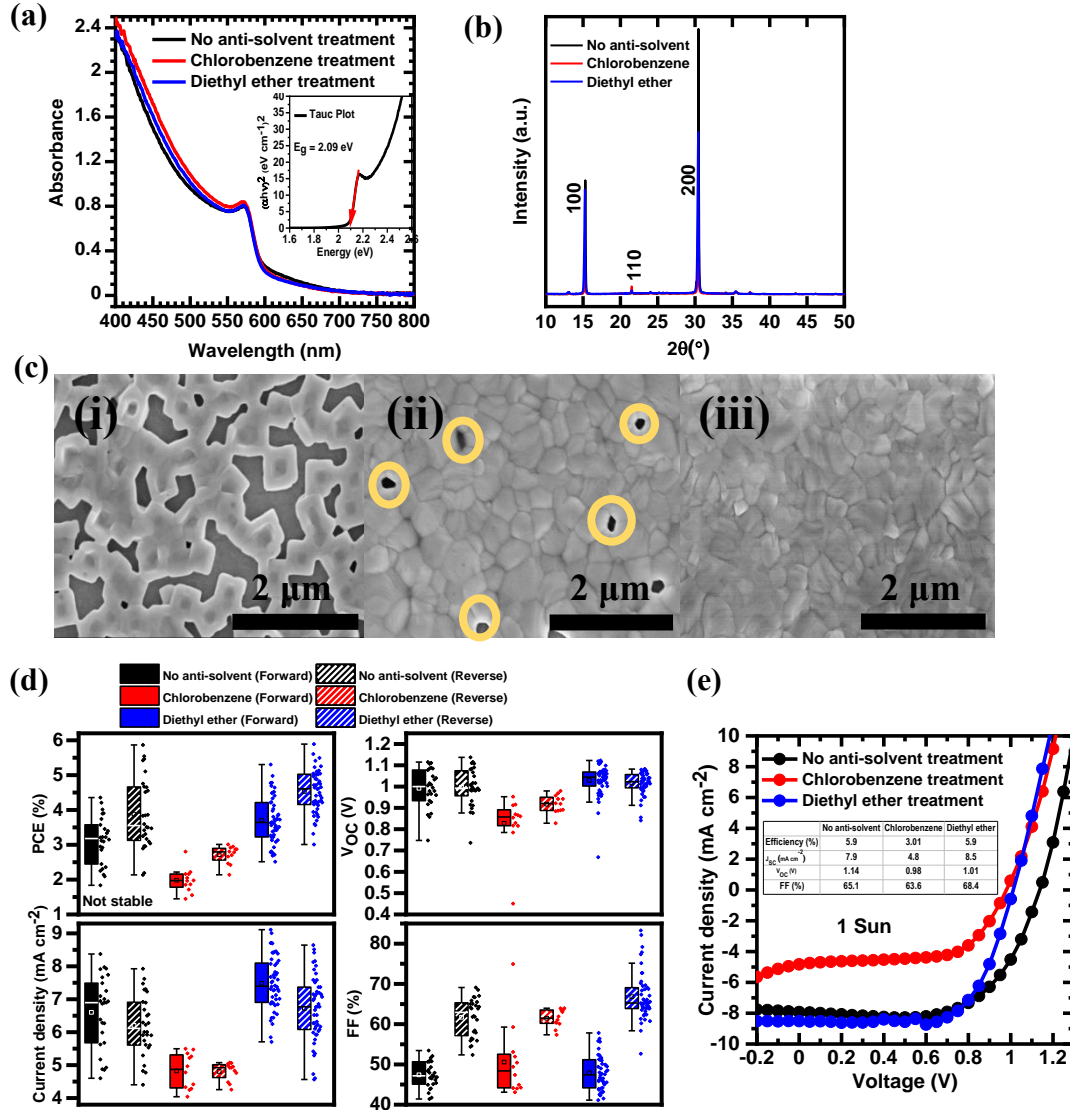


**Figure 3** (a) Absorption spectra of pristine CsPbIBr<sub>2</sub> films with no anti-solvent wash, chlorobenzene, and diethyl ether treatment (Inset is the Tauc plot showing the band gap of the CsPbIBr<sub>2</sub> perovskite film as 2.09 eV). (b) X-ray diffractograms of CsPbIBr<sub>2</sub> films fabricated without anti-solvent wash, chlorobenzene, and diethyl ether treatment. (c) Morphology studied using scanning electron microscopy of CsPbIBr<sub>2</sub> films with (i) no anti-solvent treatment, (ii) chlorobenzene (presence of pinholes shown as yellow circles), and (iii) diethyl ether treatment. (d) (Clockwise from top left) Distribution of photovoltaic parameters PCE (%),  $V_{OC}$  (V), FF (%) and  $J_{SC}$  ( $\text{mA cm}^{-2}$ ) for devices fabricated without anti-solvent treatment, with chlorobenzene, and diethyl ether in forward and reverse scans under 1 Sun. (e) Current density vs voltage curves for the best performing devices with no anti-solvent treatment,

chlorobenzene, and diethyl ether treatment along with the respective photovoltaic parameters under 1 Sun in reverse scan.

For the corresponding indoor illumination performance, devices fabricated using diethyl ether treated perovskite films showed the best efficiency under daylight white LED, recording 9.1% and 14.1% under forward and reverse scans, respectively. Though the photovoltaic parameters of these devices were comparable to those fabricated without any anti-solvent treatment (9.9% and 13.6% during forward and reverse scans, respectively), the latter devices rapidly degraded to yellow, non-perovskite phase during the measurements [Figure S2 and Table S3]. Devices fabricated using chlorobenzene treated CsPbIBr<sub>2</sub> films were not studied under low-intensity indoor illumination since they recorded the lowest photovoltaic parameters under 1 Sun and also degraded rapidly during measurement. Devices with diethyl ether treatment not only demonstrated the best device performance under both 1 Sun and indoor illumination but also enhanced air-stability compared to the other devices. Hence, the volume optimisation for anti-solvent treatment was undertaken with diethyl ether and devices fabricated with the optimised volume of 750  $\mu$ L demonstrated the champion PCE of 5.9% with low hysteresis, good repeatability of device performance, and improved air-stability. Details of the optimisation process is discussed in the Supplementary Information (Figures S3 & S4 and Table S4).

To understand the difference in photovoltaic device performance, as well as ambient stability of the diethyl ether anti-solvent treated CsPbIBr<sub>2</sub> films, detailed microstructural and spectroscopic characterisation using EBSD, XPS and Fourier transform infrared (FTIR) spectroscopy were carried out on both pristine and anti-solvent treated CsPbIBr<sub>2</sub> films and partial device heterostructures. Since the secondary electron images cannot provide any crystallographic information, EBSD measurements were performed to accurately identify crystalline grain properties (size, homogeneity and misorientation) [43].

### **(c) Microstructural and compositional analysis**

**Figures 4 (a)-(c)** show the SE images of the areas probed using EBSD, where the three samples (CsPbIBr<sub>2</sub> films) without anti-solvent, with chlorobenzene and diethyl ether treatment, respectively, were tilted by 70°. The EBSD band contrast images in **Figures 4 (d)-(f)** already indicate the grains present in the films, with grain boundaries giving lower contrast. Inverse pole figure (IPF) Z maps, as displayed in **Figures 4 (g)-(i)**, of the CsPbIBr<sub>2</sub> perovskite crystals for the three films provide the crystallographic directions in the Z direction, which is the sample normal. The sample without anti-solvent treatment showed a strong preference for the (100)

plane (or [100] direction) for crystalline grain orientation [Figure 4 (g)], whereas the (100) orientation is less dominant, with other orientations also observed in case of the films with chlorobenzene and diethyl ether treatment [Figures 4 (h) and (i), respectively]. To investigate this orientation relationship further, **Figures 4 (j)-(l)** show the pole figures of the (100) plane for the three CsPbIBr<sub>2</sub> films (note the same scale applies to all three pole figures). For the film without anti-solvent treatment, the majority of data points are at the centre of the hemisphere, confirming that most grains are (100) oriented [Figure 4 (j)]. For the samples treated with anti-solvents (chlorobenzene and diethyl ether), the spot at the centre is less dominant and additional spots appear in the respective pole figures [Figures 4 (k) and (l), respectively], compared to the films without anti-solvent treatment. **Figure S5** shows the IPF maps for the sample X, Y and Z directions for the three CsPbIBr<sub>2</sub> films, without and with anti-solvent treatment. **Figure S6** shows the same pole figures on individual scales, showing that (100) is still the dominant orientation for all samples. This agrees well with the XRD results in Figure 3 (b).

Previously Jariwala *et al.* have reported that orientational heterogeneities within the grains enhance the non-radiative recombination [38]. To unravel any crystalline orientational heterogeneity, the grain misorientation was calculated in terms of grain orientation spread (GOS) and grain reference orientation deviation (GROD) angle for all the CsPbIBr<sub>2</sub> films without and with anti-solvent treatment as seen in **Figures 4 (m)-(o)** and **Figures 4 (p)-(r)**, respectively. The GOS is the mean misorientation of a given grain, whereas the GROD angle provides the deviation of each pixel within a grain from the mean misorientation (GOS) of that grain. The mean GOS, calculated from all grains, decreases upon treatment with diethyl ether ( $0.39\pm 0.03^\circ$ ) and chlorobenzene ( $0.47\pm 0.06^\circ$ ) compared to films without any anti-solvent treatment ( $0.68\pm 0.18^\circ$ ). This can be seen in **Figure 4 (m)** for the sample without any treatment, where more grains with a larger GOS can be observed compared to the samples treated with anti-solvents which exhibit a more uniform GOS with fewer grains of larger misorientation [**Figure 4 (n)-(o)**]. The GROD angle maps in **Figures 4 (p)-(r)** show an analogous behaviour. The grains with larger mean misorientations (i.e., larger GOS) also exhibit larger GROD angle values. This implies that grains with a large GOS also possess large misorientation within their boundaries. This is most dominant for the CsPbIBr<sub>2</sub> film without anti-solvent treatment. The film with diethyl ether treatment exhibits the least amount of misorientation between grains and within a given grain compared to the other two samples. This implies that the CsPbIBr<sub>2</sub> films without anti-solvent and with chlorobenzene treatment have the highest degrees of crystalline orientational heterogeneity, and/or most likely, variation in local strain and hence,

will suffer from more non-radiative recombination. This, along with the pinholes observed in the SE images in Figure 3 (c) (ii) most likely explains the poor photovoltaic performance ( $V_{OC}$  and  $J_{SC}$ ) of CsPbIBr<sub>2</sub> devices with chlorobenzene treatment as shown in Figure 3 (e). The complete surface coverage and lowest misorientation heterogeneity of the diethyl ether treated CsPbIBr<sub>2</sub> films can thus account for the best photovoltaic device performance.

According to the previous reports, an inhomogeneous distribution of grain size can be a limiting factor of microscopic properties in halide perovskite films [43]. For the small number of grains imaged by EBSD for these three samples, no significant difference in grain size was observed. All three samples exhibit comparable mean grain sizes and grain size variability. The mean area, mean perimeter and mean circle equivalent diameter are shown in **Table S5**. The significant difference between the samples revealed by EBSD is the misorientation within the grains.



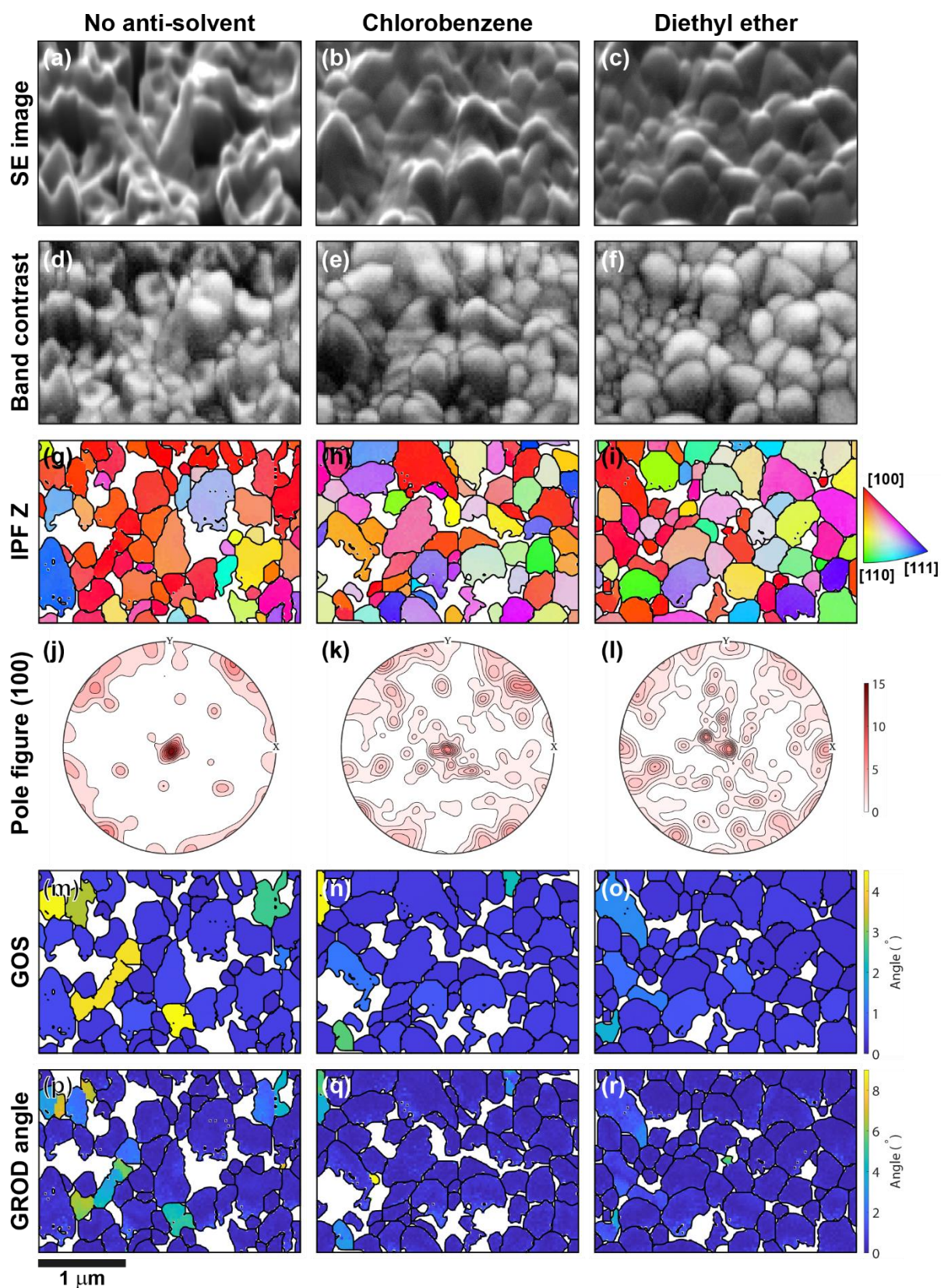


**Figure 4** SE images (a)-(c), band contrast images (d)-(f), IPF Z maps (the colour key on the right applies to all three IPF maps) (g)-(i), (100) pole figures (j)-(l), GOS maps (m)-(o) and GROD angle maps (p)-(r) derived from EBSD measurements of the CsPbIBr<sub>2</sub> films without

anti-solvent treatment (first column), with chlorobenzene (second column) and diethyl ether (third column) treatment, respectively.

The surface elemental composition and chemical states of the CsPbIBr<sub>2</sub> perovskite films on ITO, prepared without and with anti-solvent treatment, were probed using XPS to correlate the compositional features with their device performance. Clear signature peaks of Cs, Pb, I, and Br, from the CsPbIBr<sub>2</sub> films are detected with a negligible amount of carbon and without any other impurity peak which can be regarded as indicators of compositional purity of the samples (**Figure S7**) (Adventitious carbon is commonly expected in any *ex-situ* prepared sample). The high-resolution Cs 3*d*, Pb 4*f*, I 3*d* and Br 3*d* core level spectra are shown in **Figure 5**. The Cs 3*d* doublet is observed at 724.5±0.1 eV and 738.5±0.1 eV corresponding to Cs 3*d*<sub>5/2</sub> and Cs 3*d*<sub>3/2</sub> with a spin-orbit splitting of 13.9 eV [Figure 5 (a)] whereas the peaks at 138.4±0.1 eV and 143.1±0.1 eV are attributed to Pb 4*f*<sub>7/2</sub> and Pb 4*f*<sub>5/2</sub>, respectively [Figure 5 (d)]. The spectra of the two halides, i.e. iodide (I 3*d*) and bromide (Br 3*d*) are observed at 619.0±0.2 eV and 630.4±0.1 eV, assigned to I 3*d*<sub>5/2</sub> and I 3*d*<sub>3/2</sub> (splitting of 11.5 eV) [Figure 5 (b)], and at ~68.5 - 70.0 eV, respectively [Figure 5 (c)]. The peak positions and spin-orbit splitting in all the samples are very similar to the previously reported literature [9,17]. There is no appreciable variation in the Cs 3*d* and I 3*d* core levels because of treatment with different anti-solvents [**Figure 5 (a) and (b)**]. The Br 3*d* spectra have been fitted with two components corresponding to Br 3*d*<sub>5/2</sub> and Br 3*d*<sub>3/2</sub> at ~68.1 and 69.3 eV, respectively, and does not show any variation due to the different anti-solvent treatment techniques followed in this study [**Figure 5 c (i – iii)**].

The Pb 4*f* spectra for all films irrespective of preparation technique, consist of two separate contributions from 4*f*<sub>7/2</sub> and 4*f*<sub>5/2</sub> peaks with a ratio of ~1.25 and spin-orbit splitting of 4.8 eV. The primary Pb 4*f*<sub>7/2</sub> peak is found at 138.4±0.1 eV, consistent with the Pb 4*f*<sub>7/2</sub> binding energy attributed to Pb (II) in the perovskite structure [44,45]. Two smaller, yet evident peaks are detected at ~136.9±0.2 and 141.8±0.2 eV corresponding to Pb 4*f*<sub>7/2</sub> and Pb 4*f*<sub>5/2</sub>, respectively, in all samples, which can be attributed to the presence of metallic Pb (Pb<sup>0</sup>) [**Figures 5 (d) and (e)**]. This component has previously been reported as defect sites and regarded as recombination centres for the charge carriers in the perovskite film which are detrimental to device performance [45]. Though the presence of metallic Pb is observed irrespective of the sample preparation, the fraction of the Pb<sup>0</sup> signal shows significant variation depending on the anti-solvent treatment [Figure 5 (e)]. A monotonic decrease in both Pb<sup>0</sup> components (Pb<sup>0</sup> 4*f*<sub>7/2</sub> and Pb<sup>0</sup> 4*f*<sub>5/2</sub>) is observed from films without anti-solvent treatment



[Figure 5 e (i)] to those with chlorobenzene and diethyl ether treatment [Figures 5 (e) (ii) and (iii), respectively]. The quantification was performed after careful peak fitting of each component of the Pb 4*f* doublet using CasaXPS with the residue  $\chi^2 < 0.5$ . The atomic% of Pb<sup>0</sup> is 2.07% (Pb 4*f*<sub>7/2</sub>) and 1.20% (Pb 4*f*<sub>5/2</sub>) for samples without anti-solvent treatment corresponding to a Pb<sup>0</sup>/Pb<sup>2+</sup> fraction of ~0.034 which reduces to ~0.025 upon chlorobenzene treatment. In comparison, the peak intensities of metallic Pb are strikingly reduced in the films after diethyl ether treatment with the Pb<sup>0</sup>/Pb<sup>2+</sup> ratio of ~0.010, implying a much lesser defect concentration. This low metallic Pb content in diethyl ether treated CsPbIBr<sub>2</sub> films can explain the better photovoltaic performance of the corresponding devices [Table S2, Figures 3 (d) and (e)]. The evolution of metallic Pb has been previously correlated with the loss of iodine from the perovskite lattice [46]. Thus, the low content of metallic Pb in the diethyl ether treated CsPbIBr<sub>2</sub> films in turn suggests better incorporation of Pb and iodine into the lattice and correlates well with the finding from the XRD analysis (better incorporation of iodide ions into the CsPbIBr<sub>2</sub> crystal lattice).

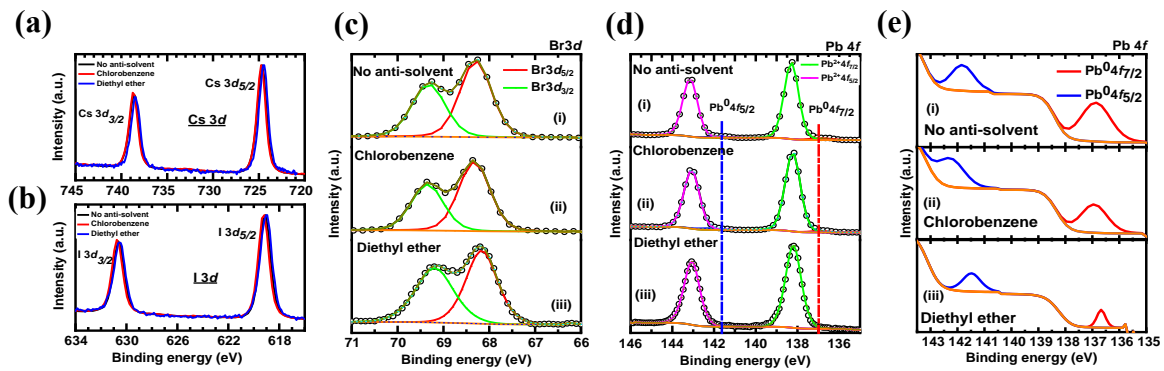


**Figure 5** High resolution XPS core level spectra (a) Cs 3*d*, (b) I 3*d*, (c) Br 3*d*, and (d) Pb 4*f* of CsPbIBr<sub>2</sub> films prepared (i) without anti-solvent treatment (ii) with chlorobenzene and (iii) diethyl ether treatment, respectively. (e) Section of the Pb 4*f* spectra showing the metallic lead (Pb<sup>0</sup> 4*f*) components only.

Though the microstructural and compositional analysis of the CsPbIBr<sub>2</sub> films prepared without and with anti-solvent treatment revealed the reason for the enhanced photovoltaic performance of devices with the diethyl ether treated CsPbIBr<sub>2</sub> films, the understanding of enhanced stability was still lacking. Hence, time-dependent stability characterisation of CsPbIBr<sub>2</sub> photovoltaic devices and partial heterostructures was carried out.

#### (d) Stability of CsPbIBr<sub>2</sub> photovoltaic devices

During 1 Sun measurements, the devices without any anti-solvent and with chlorobenzene treated CsPbIBr<sub>2</sub> films were observed to be undergoing degradation from the brown perovskite phase to the yellow non-perovskite phase. The X-ray diffraction patterns of the phase-changed CsPbIBr<sub>2</sub> film and Glass/ITO/SnO<sub>2</sub>/CsPbIBr<sub>2</sub>/Spiro-OMeTAD/Au device stack due to ageing in air are shown in **Figure S8**. The peak at 10.24° can be assigned to the  $\delta$ -phase of CsPbIBr<sub>2</sub> [10,36,47–49]. This peak is visible in both the CsPbIBr<sub>2</sub> film and the CsPbIBr<sub>2</sub> based device stack, clearly demonstrating that the freshly deposited  $\alpha$ -phase of the CsPbIBr<sub>2</sub> perovskite has degraded into the yellow non-perovskite orthorhombic  $\delta$ -phase after ageing in air. Photographs of the degraded solar cell device stack without and with different anti-solvents as observed from the Glass/ITO side are shown in Figure S9 (A/B - no anti-solvent treatment, C/D - chlorobenzene treatment, and E/F - diethyl ether treatment).

The stability of the Glass/ITO/SnO<sub>2</sub>/CsPbIBr<sub>2</sub>/Spiro-OMeTAD partial heterostructure was studied using FTIR spectroscopy to understand the role of the perovskite/Spiro-OMeTAD interface in the degradation of devices since the pristine CsPbIBr<sub>2</sub> films were very stable in ambient conditions. The degradation behaviour of the partial heterostructures was found to follow the same pattern as that of the completed photovoltaic devices with Au top electrode; that is, the CsPbIBr<sub>2</sub> perovskite phase transformed into the non-perovskite phase in less than 2 hours for the films without anti-solvent treatment whereas diethyl ether treated films were stable for longer (more than 8 hours) under humidity of 33%, with the chlorobenzene treated films in the intermediate range of hours. Previous studies have shown that the degradation observed in hybrid perovskite devices under high humidity can be assigned to the hygroscopic nature of the Li-TFSI dopant used for improving the hole mobility and conductivity of Spiro-OMeTAD hole conductor which in turn facilitates moisture ingress into the perovskite layer, thus, resulting in progressive deterioration of devices [50–52]. Detailed FTIR characterization (Supplementary Information and **Figure S10**) revealed that Spiro-OMeTAD conjugation disruption is faster in films without any anti-solvent. The rapid device degradation in devices without anti-solvent treatment can be attributed to the aggregation of hygroscopic Li<sup>+</sup> in the regions with thinner CsPbIBr<sub>2</sub> films due to the lower surface coverage than films with diethyl ether treatment. These localized regions of high moisture content would also be more susceptible to the formation of nucleation sites for the non-perovskite yellow phase due to interaction between mobile iodide species with the Spiro-OMeTAD at the hole-selective

interface [42]. Thus, the perovskite surface coverage and Spiro-OMeTAD/perovskite interface plays an important role in the ambient stability of CsPbIBr<sub>2</sub>/Spiro-OMeTAD devices.

The shelf-life stability of the unencapsulated completed device structure fabricated using diethyl ether treated CsPbIBr<sub>2</sub> was investigated. The variation in normalized PCE of these devices is shown in **Figure 6** with the inset showing the images of the devices (from both Au and Glass sides) after storage in a desiccator (humidity ~30%) for 40 days. The measurements of these un-encapsulated devices were carried out in ambient air under relative humidity (RH) of 33%, every couple of days for 64 days. Between measurements, the devices were stored in the dark at RH of ~30%. The devices retained >55% of their maximum PCE after 40 days of storage which slightly reduced to 51% after two months. This kind of stability value is one of the best reported so far for CsPbIBr<sub>2</sub> films since most of the studies report device storage under nitrogen and controlled humidity conditions. Hence, this study establishes the efficacy of the anti-solvent treatment technique with diethyl ether for improving device stability by defect passivation and reduction in grain misorientation. Preliminary attempts were made to use these CsPbIBr<sub>2</sub> devices for powering a non-inverting buffer with open-drain output under indoor light (0.25 mW cm<sup>-2</sup>) as discussed in the Supplementary Information (**Figure S11**).

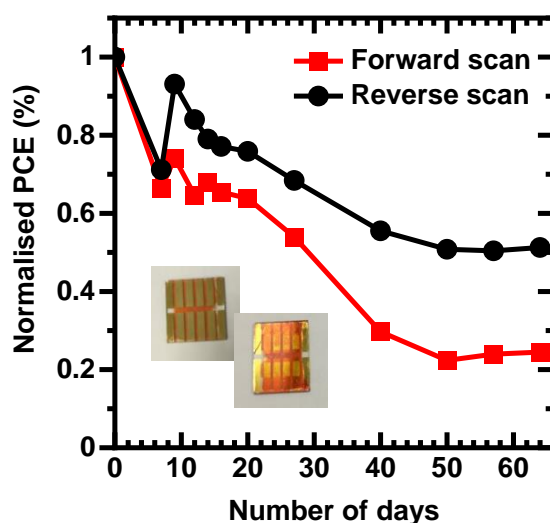


**Figure 6** Variation in normalized power conversion efficiency of the optimized CsPbIBr<sub>2</sub> perovskite solar cells studied as a function of the number of days; inset shows the photographs of the diethyl treated CsPbIBr<sub>2</sub> based devices after 40 days storage in RH 30%.

## 4. Conclusions

In summary, highly crystalline and compact CsPbIBr<sub>2</sub> perovskite based photovoltaic devices were fabricated in n-i-p configuration with a PCE of 14.1% under indoor illumination at 1000 lux illuminance. Detailed investigation of the surface morphology demonstrated that the selection of anti-solvent was of critical importance in obtaining the desired dense and compact CsPbIBr<sub>2</sub> perovskite morphology with excellent surface coverage and improved air-stability of the devices. In-depth microstructural characterisation undertaken in this study revealed that diethyl ether anti-solvent treatment was effective in reducing the defect concentration in the form of metallic Pb, and in suppressing the grain misorientation in CsPbIBr<sub>2</sub> films which resulted in improved performance of the corresponding photovoltaic devices. The optimised devices also retained >55% of the maximum PCE after storage in 30% relative humidity for more than 40 days. The ambient stability of CsPbIBr<sub>2</sub>/Spiro-OMeTAD devices was influenced by the perovskite surface coverage as well as the Spiro-OMeTAD/perovskite interface. The low temperature annealed, efficient and stable all-inorganic CsPbIBr<sub>2</sub> perovskites developed in this study not only shows promise of compatibility with flexible and wearable substrates but also for powering next-generation electronic devices in the IoT.

## Data Accessibility

The research data underpinning this publication can be accessed at <https://doi.org/10.17630/970ac996-d043-48f8-bf70-7c0eb33f7b9a> [REF].

## CRedit authorship contribution statement

Paheli Ghosh: Methodology, Investigation, Data Acquisition, Formal analysis, Data curation, Writing - original draft, Writing - review & editing. Jochen Bruckbauer: Acquisition, Investigation, and Analysis of EBSD data, Writing - original draft (section on EBSD), Writing - review & editing. Carol Trager-Cowan: Acquisition, Investigation, and Analysis of EBSD data, Writing - review & editing. Lethy Krishnan Jagadamma: Conceptualization, Methodology, Data Acquisition, Formal analysis, Writing - original draft, Writing - review & editing, Supervision, Funding acquisition, Project administration.

## Declaration of competing interest

The authors declare that they have no known competing financial or other interests that could have appeared to influence the work reported in this paper.

## Acknowledgement

LKJ acknowledges funding from UKRI-FLF through MR/T022094/1. LKJ acknowledges Professor Ifor D. W. Samuel and Professor Graham A. Turnbull for the kind permission to access 1 Sun and EQE measurements. LKJ and PG acknowledge Dr Ben F. Spencer for the XPS data acquisition, which was supported by the Henry Royce Institute, funded through UK EPSRC grants EP/R00661X/1, EP/P025021/1 and EP/P025498/1 and Dr Julia L. Payne for the arrangements with XRD and FTIR measurements. JB and CTC acknowledge funding from UK EPSRC grant EP/P015719/1.

## References

- [1] K. Ruhle, M. Kasemann, Approaching high efficiency wide range silicon solar cells, *Conf. Rec. IEEE Photovolt. Spec. Conf.* (2013) 2651–2654.
- [2] I. Raifuku, Y. Ishikawa, S. Ito, Y. Uraoka, Characteristics of Perovskite Solar Cells under Low-Illuminance Conditions, *J. Phys. Chem. C*. 120 (2016) 18986–18990.
- [3] H.K.H. Lee, J. Barbé, W.C. Tsoi, *Organic and perovskite photovoltaics for indoor applications*, Elsevier Ltd, 2019.
- [4] M.F. Müller, M. Freunek, L.M. Reindl, Maximum efficiencies of indoor photovoltaic devices, *IEEE J. Photovoltaics*. 3 (2013) 59–64.
- [5] J.K.W. Ho, H. Yin, S.K. So, From 33% to 57%-An elevated potential of efficiency limit for indoor photovoltaics, *J. Mater. Chem. A*. 8 (2020) 1717–1723.
- [6] NREL, *Best Research Cell Efficiencies*, (2021).
- [7] J. Zhang, G. Hodes, Z. Jin, S. Liu, All-Inorganic CsPbX<sub>3</sub> Perovskite Solar Cells: Progress and Prospects, *Angew. Chemie - Int. Ed.* 58 (2019) 15596–15618.
- [8] W. Xiang, W. Tress, Review on Recent Progress of All-Inorganic Metal Halide Perovskites and Solar Cells, *Adv. Mater.* 31 (2019) 1902851.
- [9] Q. Ma, S. Huang, X. Wen, M.A. Green, A.W.Y. Ho-Baillie, Hole Transport Layer Free Inorganic CsPbIBr<sub>2</sub> Perovskite Solar Cell by Dual Source Thermal Evaporation, *Adv. Energy Mater.* 6 (2016) 2–6.
- [10] J. Lin, M. Lai, L. Dou, C.S. Kley, H. Chen, F. Peng, J. Sun, D. Lu, S.A. Hawks, C. Xie, F. Cui, A.P. Alivisatos, D.T. Limmer, P. Yang, Thermochromic halide perovskite solar cells, *Nat. Mater.* 17 (2018) 261–267.
- [11] V.O. Eze, G.R. Adams, L. Braga Carani, R.J. Simpson, O.I. Okoli, Enhanced Inorganic CsPbIBr<sub>2</sub> Perovskite Film for a Sensitive and Rapid Response Self-Powered Photodetector, *J. Phys. Chem. C*. 124 (2020) 20643–20653.
- [12] G.O. Interlayer, Z. Zhang, W. Zhang, Q. Jiang, Z. Wei, Y. Zhang, H.L. You, High-Performance, Vacuum-Free, and Self-Powered CsPbIBr<sub>2</sub> Photodetectors Boosted by Ultra-Wide-Bandgap Ga<sub>2</sub>O<sub>3</sub> Interlayer, *IEEE Electron Device Lett.* 41 (2020) 1532–1535.

- [13] Z. Zhang, W. Zhang, Q. Jiang, Z. Wei, M. Deng, D. Chen, W. Zhu, J. Zhang, H. You, Toward High-Performance Electron/Hole-Transporting-Layer-Free, Self-Powered CsPbIBr<sub>2</sub> Photodetectors via Interfacial Engineering, *ACS Appl. Mater. Interfaces*. 12 (2020) 6607–6614.
- [14] S.L. Zhang, Ting, Self-Powered All-Inorganic Perovskite Photodetectors with Fast Response Speed, *Nanoscale Res. Lett.* (2021) 1–13.
- [15] Y. Su, X. Chen, W. Ji, Q. Zeng, Z. Ren, Z. Su, L. Liu, Highly Controllable and Efficient Synthesis of Mixed-Halide CsPbX<sub>3</sub> (X = Cl, Br, I) Perovskite QDs toward the Tunability of Entire Visible Light, *ACS Appl. Mater. Interfaces*. 9 (2017) 33020–33028.
- [16] C.F.J. Lau, X. Deng, Q. Ma, J. Zheng, J.S. Yun, M.A. Green, S. Huang, A.W.Y. Ho-Baillie, CsPbIBr<sub>2</sub> Perovskite Solar Cell by Spray-Assisted Deposition, *ACS Energy Lett.* 1 (2016) 573–577.
- [17] J. Liang, P. Zhao, C. Wang, Y. Wang, Y. Hu, G. Zhu, L. Ma, J. Liu, Z. Jin, CsPb<sub>0.9</sub>Sn<sub>0.1</sub>IBr<sub>2</sub> Based All-Inorganic Perovskite Solar Cells with Exceptional Efficiency and Stability, *J. Am. Chem. Soc.* 139 (2017) 14009–14012.
- [18] W. Li, M.U. Rothmann, A. Liu, Z. Wang, Y. Zhang, A.R. Pascoe, J. Lu, L. Jiang, Y. Chen, F. Huang, Y. Peng, Q. Bao, J. Etheridge, U. Bach, Y.-B.B. Cheng, Phase Segregation Enhanced Ion Movement in Efficient Inorganic CsPbIBr<sub>2</sub> Solar Cells, *Adv. Energy Mater.* 7 (2017) 1700946.
- [19] M. Aamir, T. Adhikari, M. Sher, N. Revaprasadu, W. Khalid, J. Akhtar, J.M. Nunzi, Fabrication of planar heterojunction CsPbBr<sub>2</sub>I perovskite solar cells using ZnO as an electron transport layer and improved solar energy conversion efficiency, *New J. Chem.* 42 (2018) 14104–14110.
- [20] J. Liang, Z. Liu, L. Qiu, Z. Hawash, L. Meng, Z. Wu, Y. Jiang, L.K. Ono, Y. Qi, Enhancing Optical, Electronic, Crystalline, and Morphological Properties of Cesium Lead Halide by Mn Substitution for High-Stability All-Inorganic Perovskite Solar Cells with Carbon Electrodes, *Adv. Energy Mater.* 8 (2018) 1–7.
- [21] W. Zhu, Q. Zhang, D. Chen, Z. Zhang, Z. Lin, J. Chang, J. Zhang, C. Zhang, Y. Hao, Intermolecular Exchange Boosts Efficiency of Air-Stable, Carbon-Based All-Inorganic Planar CsPbIBr<sub>2</sub> Perovskite Solar Cells to Over 9%, *Adv. Energy Mater.* 8 (2018) 1–11.
- [22] W.S. Subhani, K. Wang, M. Du, X. Wang, S. (Frank) Liu, Interface-Modification-Induced Gradient Energy Band for Highly Efficient CsPbIBr<sub>2</sub> Perovskite Solar Cells, *Adv. Energy Mater.* 9 (2019) 1–9.
- [23] W. Zhu, Z. Zhang, W. Chai, Q. Zhang, D. Chen, Z. Lin, J. Chang, J. Zhang, C. Zhang, Y. Hao, Band Alignment Engineering Towards High Efficiency Carbon-Based Inorganic Planar CsPbIBr<sub>2</sub> Perovskite Solar Cells, *ChemSusChem*. 12 (2019) 2318–2325.
- [24] Q. Zhang, W. Zhu, D. Chen, Z. Zhang, Z. Lin, J. Chang, J. Zhang, C. Zhang, Y. Hao, Light Processing Enables Efficient Carbon-Based, All-Inorganic Planar CsPbIBr<sub>2</sub> Solar Cells with High Photovoltages, *ACS Appl. Mater. Interfaces*. 11 (2019) 2997–3005.
- [25] Y. Guo, X. Yin, J. Liu, W. Que, Highly efficient CsPbIBr<sub>2</sub> perovskite solar cells with efficiency over 9.8% fabricated using a preheating-assisted spin-coating method, *J.*

- Mater. Chem. A. 7 (2019) 19008–19016.
- [26] Y. Peng, T.N. Huq, J. Mei, L. Portilla, R.A. Jagt, L.G. Occhipinti, J.L. MacManus-Driscoll, R.L.Z. Hoye, V. Pecunia, Lead-Free Perovskite-Inspired Absorbers for Indoor Photovoltaics, *Adv. Energy Mater.* 2002761 (2020) 1–12.
- [27] Z. Guo, A.K. Jena, I. Takei, M. Ikegami, A. Ishii, Y. Numata, N. Shibayama, T. Miyasaka, Dopant-Free Polymer HTM-Based CsPbI<sub>2</sub>Br Solar Cells with Efficiency Over 17 % in Sunlight and 34 % in Indoor Light, *Adv. Funct. Mater.* 2103614 (2021) 1–9.
- [28] B. Parida, I.S. Jin, J.W. Jung, Dual Passivation of SnO<sub>2</sub> by Tetramethylammonium Chloride for High-Performance CsPbI<sub>2</sub>Br-Based Inorganic Perovskite Solar Cells, *Chem. Mater.* 33 (2021) 5850–5858.
- [29] I. Su Jin, K. Su, J. Woong, CsCl-induced defect control of CsPbI<sub>2</sub>Br thin films for achieving open-circuit voltage of 1.33 V in all-inorganic perovskite solar cells, *J. Power Sources.* 512 (2021) 230481.
- [30] GitHub - mtex-toolbox/mtex\_ MTEX is a free Matlab toolbox for quantitative texture analysis, (n.d.). <https://github.com/mtex-toolbox/mtex>.
- [31] N. Fairley, CasaXPS, (2019).
- [32] J.J. Zhou, R.Z. Ding, Y.Q. Peng, C.F. Gu, Z.L. Zhou, W.L. Lv, S.N. Xu, L. Sun, Y. Wei, Y. Wang, Light illumination and temperature-induced current–voltage hysteresis in single-crystal perovskite photodiodes, *CrystEngComm.* 23 (2021) 1663–1670.
- [33] B. Yang, M. Wang, X. Hu, T. Zhou, Z. Zang, Highly efficient semitransparent CsPbI<sub>2</sub>Br<sub>2</sub> perovskite solar cells via low-temperature processed In<sub>2</sub>S<sub>3</sub> as electron-transport-layer, *Nano Energy.* 57 (2019) 718–727.
- [34] J. Pan, X. Zhang, Y. Zheng, W. Xiang, Morphology control of perovskite film for efficient CsPbI<sub>2</sub>Br<sub>2</sub> based inorganic perovskite solar cells, *Sol. Energy Mater. Sol. Cells.* 221 (2021) 110878.
- [35] C. Liu, W. Li, J. Chen, J. Fan, Y. Mai, R.E.I. Schropp, Ultra-thin MoO<sub>x</sub> as cathode buffer layer for the improvement of all-inorganic CsPbI<sub>2</sub>Br<sub>2</sub> perovskite solar cells, *Nano Energy.* 41 (2017) 75–83.
- [36] Y. Guo, F. Zhao, Z. Li, J. Tao, D. Zheng, J. Jiang, J. Chu, Growth control and defect passivation toward efficient and low-temperature processed carbon based CsPbI<sub>2</sub>Br<sub>2</sub> solar cell, *Org. Electron.* 83 (2020) 105731.
- [37] B.R. Yongtao Liu, Liam Collins, Roger Proksch, Songkil Kim, Watson, A. V. Doughty, Benjamin, , Tessa R. Calhoun, Mahshid Ahmadi, Ievlev, B.H. and O.S.O. Jesse, Stephen, Scott T. Retterer, Alex Belianinov, Xiao, Kai, Jingsong Huang, Bobby G. Sumpter, Sergei V. Kalinin, Chemical nature of ferroelastic twin domains in CH<sub>3</sub>NH<sub>3</sub>PbI<sub>3</sub> perovskite, *Nat. Mater.* 17 (2018) 1013–1019.
- [38] S. Jariwala, H. Sun, E.C. Garnett, S. David, S. Jariwala, H. Sun, G.W.P. Adhyaksa, A. Lof, L.A. Muscarella, Local Crystal Misorientation Influences Non-radiative Recombination in Halide Perovskites Local Crystal Misorientation Influences Non-radiative Recombination in Halide Perovskites, *Joule.* 3 (2019) 3048–3060.
- [39] Y. Li, Y. Wang, T. Zhang, S. Yoriya, P. Kumnorkaew, S. Chen, X. Guo, Y. Zhao, Li

- dopant induces moisture sensitive phase degradation of an all-inorganic CsPbI<sub>2</sub>Br perovskite, *Chem. Commun.* 54 (2018) 9809–9812.
- [40] Z. Hawash, L.K. Ono, S.R. Raga, M. V. Lee, Y. Qi, Air-exposure induced dopant redistribution and energy level shifts in spin-coated Spiro-Meotad films, *Chem. Mater.* 27 (2015) 562–569.
- [41] E.J. Juárez-Pérez, M.R. Leyden, S. Wang, L.K. Ono, Z. Hawash, Y. Qi, Role of the Dopants on the Morphological and Transport Properties of Spiro-MeOTAD Hole Transport Layer, *Chem. Mater.* 28 (2016) 5702–5709.
- [42] S.A.L. Weber, I.M. Hermes, S.-H. Turren-Cruz, C. Gort, V.W. Bergmann, L. Gilson, A. Hagfeldt, M. Graetzel, W. Tress, R. Diger Berger, How the formation of interfacial charge causes hysteresis in perovskite solar cells, *Energy Environ. Sci.* 11 (2018) 2404–2413.
- [43] H. Sun, G.W.P. Adhyaksa, E.C. Garnett, The Application of Electron Backscatter Diffraction on Halide Perovskite Materials, *Adv. Energy Mater.* 10 (2020) 2000364.
- [44] R. Lindblad, D. Bi, B. Park, J. Oscarsson, M. Gorgoi, H. Siegbahn, M. Odelius, E.M.J. Johansson, Electronic Structure of TiO<sub>2</sub>/CH<sub>3</sub>NH<sub>3</sub>PbI<sub>3</sub> Perovskite Solar Cell Interfaces, *J. Phys. Chem. Lett.* 4 (2014) 648.
- [45] G. Sadoughi, D.E. Starr, E. Handick, S.D. Stranks, M. Gorgoi, R.G. Wilks, M. Baer, H.J. Snaith, Observation and Mediation of the Presence of Metallic Lead in Organic-Inorganic Perovskite Films, *ACS Appl. Mater. Interfaces.* 7 (2015) 13440–13444.
- [46] J.D. Mcgettrick, K. Hooper, A. Pockett, J. Baker, J. Troughton, M. Carnie, T. Watson, Sources of Pb (0) artefacts during XPS analysis of lead halide perovskites, *Mater. Lett.* 251 (2019) 98–101.
- [47] J.K. Nam, M.S. Jung, S.U. Chai, Y.J. Choi, D. Kim, J.H. Park, Unveiling the Crystal Formation of Cesium Lead Mixed-Halide Perovskites for Efficient and Stable Solar Cells, *J. Phys. Chem. Lett.* 8 (2017) 2936–2940.
- [48] C. Liu, W. Li, H. Li, H. Wang, C. Zhang, Y. Yang, X. Gao, Q. Xue, H.L. Yip, J. Fan, R.E.I. Schropp, Y. Mai, Structurally Reconstructed CsPbI<sub>2</sub>Br Perovskite for Highly Stable and Square-Centimeter All-Inorganic Perovskite Solar Cells, *Adv. Energy Mater.* 9 (2019) 1803572.
- [49] H. Wang, H. Li, S. Cao, M. Wang, J. Chen, Z. Zang, Interface Modulator of Ultrathin Magnesium Oxide for Low-Temperature-Processed Inorganic CsPbIBr<sub>2</sub> Perovskite Solar Cells with Efficiency Over 11%, *Sol. RRL.* 2000226 (2020) 1–11.
- [50] S.N. Habisreutinger, T. Leijtens, G.E. Eperon, S.D. Stranks, R.J. Nicholas, H.J. Snaith, Carbon Nanotube/Polymer Composites as a Highly Stable Hole Collection Layer in Perovskite Solar Cells, *Nano Lett.* 14 (2014) 5561–5568.
- [51] J. Liu, S. Pathak, T. Stergiopoulos, T. Leijtens, K. Wojciechowski, S. Schumann, N. Kausch-busies, H.J. Snaith, Employing PEDOT as the p - Type Charge Collection Layer in Regular Organic – Inorganic Perovskite Solar Cells, *J. Phys. Chem. Lett.* 6 (2015) 1666–1673.
- [52] A. Pellaroque, N.K. Noel, S.N. Habisreutinger, Y. Zhang, S. Barlow, S.R. Marder, H.J. Snaith, Efficient and Stable Perovskite Solar Cells Using Molybdenum Tris(dithiolene)s as p-Dopants for Spiro-OMeTAD, *ACS Energy Lett.* 2 (2017) 2044–2050.